Rippling, buckling, and melting of single- and multilayer MoS_2

Sandeep Kumar Singh,[1] M. Neek-Amal,[1,2] S. Costamagna,[1,3] and F. M. Peeters[1]

[1]*Universiteit Antwerpen, Department of Physics, Groenenborgerlaan 171, BE-2020 Antwerpen, Belgium*

[2]*Department of Physics, Shahid Rajaee Teacher Training University, Lavizan, Tehran 16785-136, Iran*

[3]*Facultad de Ciencias Exactas Ingeniería y Agrimensura, Universidad Nacional de Rosario and Instituto de Física Rosario, Bv. 27 de Febrero 210 bis, 2000 Rosario, Argentina*

(Received 1 October 2014; revised manuscript received 3 December 2014; published 5 January 2015)

Large-scale atomistic simulations using the reactive empirical bond order force field approach is implemented to investigate thermal and mechanical properties of single-layer (SL) and multilayer (ML) molybdenum disulfide (MoS_2). The amplitude of the intrinsic ripples of SL MoS_2 are found to be smaller than those exhibited by graphene (GE). Furthermore, because of the van der Waals interaction between layers, the out-of-plane thermal fluctuations of ML MoS_2 decreases rapidly with increasing number of layers. This trend is confirmed by the buckling transition due to uniaxial stress which occurs for a significantly larger applied tension as compared to graphene. For SL MoS_2, the melting temperature is estimated to be 3700 K which occurs through dimerization followed by the formation of small molecules consisting of two to five atoms. When different types of vacancies are inserted in the SL MoS_2 it results in a decrease of both the melting temperature as well as the stiffness.

DOI: 10.1103/PhysRevB.91.014101 PACS number(s): 68.60.Dv, 62.20.−x

I. INTRODUCTION

Two-dimensional (2D) transition-metal dichalcogenides (TMDCs) have attracted a lot of attention due to the wide range of electronic phases that they can exhibit, ranging from metallic [1–3], semiconductor [4–6], to superconductor [7]. Recently, a lot of research efforts were devoted to MoS_2 due to its wide availability in nature as molybdenite and its promising semiconducting characteristics (in contrast to graphene which has a zero band gap). Bulk MoS_2 has an indirect band gap [8] whereas its single layer (SL) has a direct band gap [9] and exhibits photoluminescence [10] which is advantage for optoelectronic applications. While it is known that the band gap can be tuned by lattice deformations [11], the microscopic details of MoS_2 under applied strain are still not well understood.

The phonon spectrum of MoS_2 is very different from that of graphene, resulting in distinct structural and thermal properties, e.g., the well-known negative thermal expansion of graphene is not observed in MoS_2 [12]. There is also an energy gap of $\sim$50 cm^{-1} in the phonon spectrum of MoS_2 which separates optical and acoustic phonon bands. The knowledge of the thermomechanical properties of MoS_2 is crucial for the enhancement of the performance of devices based on MoS_2. The role of defects on the physical properties of monolayer MoS_2 is also important because most of the 2D materials contain vacancies, which are generated during the growth process [13,14] or by ballistic displacements during imaging such as electron irradiation, due to chemical etching and electron excitations in high-resolution transmission electron microscopy [15–19]. Recently, Zhou *et al.* [20] found six types of point defects in monolayer MoS_2 grown by chemical vapor deposition: (i) monosulfur vacancy (V_S), (ii) disulfur vacancy (V_{S2}), (iii) vacancy complex of Mo and three nearby sulfurs (V_{MoS3}), (iv) vacancy complex of Mo nearby three disulfur pairs (V_{MoS6}), and (v) antisite defects where a Mo atom substitutes a S_2 column (Mo_{S2}) or (vi) a S_2 column substituting a Mo atom ($S2_{Mo}$).

In our previous studies we investigated the thermomechanical properties of different 2D materials, e.g., graphene (GE), hexagonal boron-nitride (h-BN), and their functionalized structures [21–23]. Here we report on the thermomechanical properties of single- and multilayer MoS_2. Due to the S-Mo-S sandwich structure (see Fig. 1), we found exceptional mechanical stability and a lower thermally excited rippling behavior as compared with graphene. Similarly, the melting of MoS_2 occurs also at a lower temperature and exhibits different microscopical characteristics, such as the formation of small molecules.

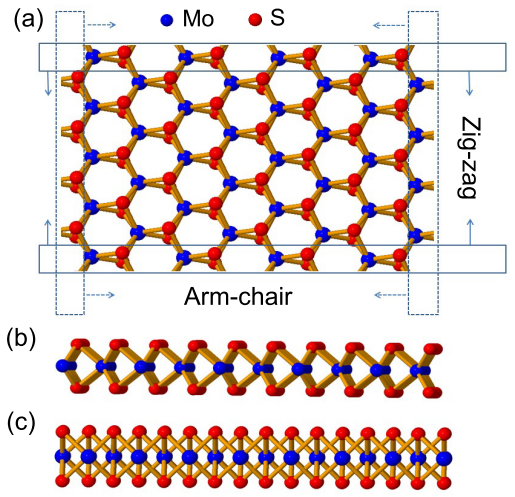

FIG. 1. (Color online) Schematic (a) top, (b) arm-chair, and (c) zigzag side views of single-layer MoS_2. Big-blue (small-red) circles refer to the Mo (S) atoms. Dashed rectangles in (a) indicate the atoms that are fixed during compression.

The paper is organized as follows: Details of the molecular-dynamics (MD) simulation and a description of the modified Lindemann parameter used to detect the melting transition are described in Sec. II. Then, in Sec. III we present results for the thermal ripples and we compare them with those of GE. In Sec. IV we obtain the buckling transition for applied stress in the zigzag and arm-chair directions. We discus the melting behavior of MoS_2 together with the effect of several kinds of

vacancies on it in Sec. V. Finally, in Sec. VI we present the conclusions of our work.

II. SIMULATION METHOD

A proper interatomic potential function which is capable of describing accurately the interactions in the material system is of crucial importance. Recently, a new approach based on bond-order potentials emerged that depend on the local chemical environment in reactive simulations which capture bond formation and breaking, saturated and unsaturated bonds, dangling and radical bonds, as well as single, double, or triple bonds. Liang *et al.* [24–26] presented an interatomic potential for Mo-S systems which contains a many-body reactive empirical bond-order (REBO) potential [27] with a two-body Lennard–Jones (LJ) potential. The REBO potential was chosen because it allows for bond breaking and bond formation during simulation. The parametrized many-body Mo-S potential energy focuses primarily on the structural and elastic properties of MoS_2 maintaining its transferability to other systems such as pure Mo structures, low coordinated S, and some other binary structures.

The Mo-S many-body empirical potential has the following analytical form:

$$E_b = \frac{1}{2}\sum_i \sum_{j(>i)} [V^R(r_{ij}) - b_{ij} V^A(r_{ij})]. \quad (1)$$

Here, E_b is the total binding energy, $V^R(r_{ij})$ and $V^A(r_{ij})$ are a repulsive and an attractive term, respectively, with r_{ij} being the distance between atoms i and j and given by

$$V^R(r) = f^C(r)(1 + Q/r)Ae^{-\alpha r}, \quad (2)$$

$$V^A(r) = f^C(r)\sum_{n=1}^{3} B_n e^{-\beta r}, \quad (3)$$

where the cutoff function $f^C(r)$ is taken from the switching cutoff scheme. The values for all the parameters used in our calculation for the Mo-S potential can be found in Refs. [24,25] and are therefore not listed here. Alternatively, it is also possible to use its competitor, the Stillinger–Weber potential, to model the interaction between Mo-S, Mo-Mo, and S-S [28].

The mutual interaction between different S-Mo-S trilayers is a van der Waals (vdW) attraction between the S atoms which we describe by the well-known Lennard–Jones potential,

$$E_{LJ}(r) = 4\epsilon\left[\left(\frac{\sigma}{r}\right)^{12} - \left(\frac{\sigma}{r}\right)^{6}\right], \quad (4)$$

where r is the interatomic distance between S-S atoms, $\sigma = 3.3$ Å, and $\epsilon = 6.93$ meV. The 12-6 Lennard–Jones potential parameters are used for the S-S interaction such that the elastic constant c_{33} of MoS_2 bulk is correctly reproduced [24].

In the next section we study the thermal rippling, the mechanical properties, and the melting of a single- and bilayer of MoS_2 by using large scale atomistic simulations with the above potentials. The Mo-S parameters were implemented in Large-scale Atomic/Molecular Massively Parallel Simulator package LAMMPS [29,30].

To account for the melting transition we analyzed the variation of the total potential energy E_T per atom with temperature identifying partial contributions from Mo atoms (E_{Mo}) and S atoms (E_S). The Lindemann criterion [31], which states that the system is melted when the root-mean-square (rms) value of the atomic displacement is of the order of a tenth of the lattice constant, was used to characterize the ordered state by considering the modified parameter γ, used previously for 2D systems [32–34] and defined as

$$\gamma = \frac{1}{a^2}\left\langle \left| \mathbf{r}_i - \frac{1}{n}\sum_j \mathbf{r}_j \right|^2 \right\rangle, \quad (5)$$

where $a = 1/\sqrt{\pi\rho_0}$, ρ_0 is the 2D particle density at $T = 0$ K, n is the number of nearest-neighbor atoms, $\mathbf{r}_i$ is the position of the ith atom, and the sum over j runs over the nearest-neighbor atoms. Here, i and j were restricted to run only over Mo atoms.

III. INTRINSIC RIPPLES

In order to study the thermal stability of MoS_2 we considered a square-shaped computational unit cell of MoS_2 ($l_x = 260$ Å, $l_y = 280$ Å) with both arm-chair and zigzag edges in the x and y directions with a total number of $N = 25\,920$ atoms in the single-layer and $N = 51\,840$ atoms in bilayer MoS_2. In our simulation we adopted periodic boundary conditions and employed the isothermal-isobaric (NPT) ensemble with $P = 0$ using the Nosé–Hoover thermostat and varied the temperature from 10 to 900 K.

In Fig. 2(a) we show the evolution with temperature of the average value of the height fluctuations $\langle h^2 \rangle$ where h refers to the height of the Mo atoms with respect to the center of mass of the central Mo layer. For comparison we added here the results of single-layer graphene (circles) of comparable system size. Notice that, in the whole temperature range, $\langle h^2 \rangle$ for single-layer MoS_2 is smaller than that of graphene. This result agrees with the estimated mechanical properties of these materials where MoS_2 is expected to be more rigid [25]. Notice that, while the distance between the Mo atoms in the Mo layer is larger than that of the C atoms in graphene, it is the Mo-S interaction that suppresses the height fluctuations of the Mo atoms in MoS_2.

When a second layer of MoS_2 is added to form bilayer MoS_2, $\langle h^2 \rangle$ is strongly reduced. This effect, due to the S-S van der Waals-type interaction acting between the S layers,

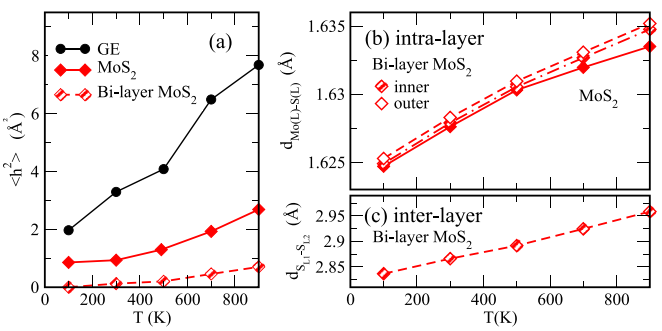

FIG. 2. (Color online) (a) Variation of $\langle h^2 \rangle$ with temperature of single-layer MoS_2, bilayer MoS_2, and graphene. (b) Mo-S and (c) S-S bond lengths versus temperature.

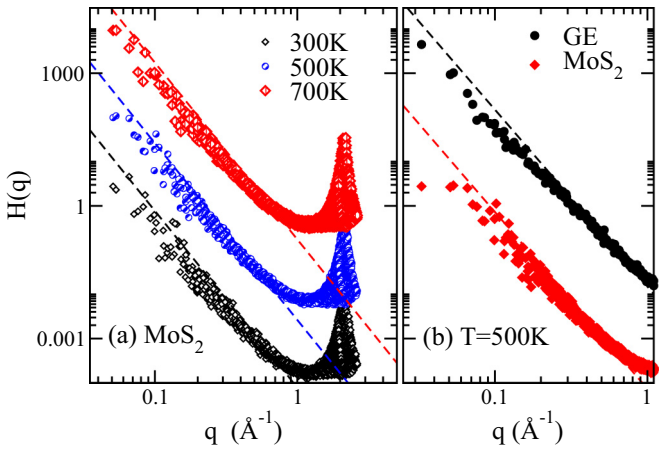

FIG. 3. (Color online) (a) Height-height correlation function for MoS_2 at three different temperatures. (b) Comparison of H(q) between GE and MoS_2 at 500 K.

is fundamentally different from the Mo-S interaction. The temperature dependence of the intralayer Mo-S and interlayer S-S (for bilayer MoS_2) distances are shown in Figs. 2(b) and 2(c), respectively. Notice that the distance Mo-S in bilayer MoS_2 is slightly larger than that of the single layer and that there exists a small difference between the S atoms from the inner and the outer side which are more free to move.

The most adequate theory which allows us to analyze in more depth the behavior of the intrinsic ripples is the elastic theory of continuum membranes [35]. Its use permits the detection of ripples with particular wavelengths and also an estimation of the anharmonic interactions in the system. The key quantity which characterizes the behavior of the out-of-plane thermal fluctuations is the height-height correlation function which, in the harmonic limit, has the following power law behavior $H(q) = \langle h(q)^2 \rangle \approx q^{-4}$. The out-of-plane displacements of Mo atoms was analyzed by calculating $H(q)$ from our molecular dynamics simulation by following the same procedure as explained in our previous works [21,22].

In Fig. 3 we show $H(q)$ at 300, 500, and 700 K for single-layer MoS_2. The results are shifted for a better comparison. The dashed lines correspond to the harmonic behavior and the peaked structures at large wavelength are the Bragg peaks of the crystalline lattice of the Mo layer. In all cases $H(q)$ follows closely the q^{-4} law. In the long-wavelength regime, however, a larger fluctuation of the points together with a deviation from the harmonic curve is observed.

In the case of GE, the stability of the membrane has been ascribed to the anharmonic coupling between the in-plane and out-of-plane modes which renormalizes the long-wavelength ripples and prevents the occurrence of the crumpling transition [36,37]. In Fig. 3(b) we show $H(q)$ for GE together with the one obtained for MoS_2, at 500 K. While $H(q)$ in GE exhibits the expected deviation from the q^{-4} harmonic scaling due to the anharmonic interactions at small q, in MoS_2 a larger fluctuation in the simulation results is present. However, in the long-wavelength regime a deviation from the harmonic law still exists and appears to be larger than that in GE. This result is consistent with the lower value of $\langle h^2 \rangle$ reported in Fig. 2(a) which is a consequence of the reduction in long-wavelength ripples.

The origin of the breakdown of the harmonic behavior in MoS_2 is very different from the one in GE. Because of the layered structure of MoS_2, its phonon modes and lattice vibration are different from those in single-layer graphene. The internal modes (due to the vibration of the Mo-S bonds) are activated with lower energy with respect to, e.g., the C–C bonds in graphene. The latter is more susceptible to temperature, making it a more floppy material. This can be seen also from the results of next section where we investigate the buckling transition. Therefore, we expect less coupling between out-of-plane and in-plane modes in MoS_2 as compared with graphene.

IV. BUCKLING TRANSITION

The specific crystal structure of MoS_2 influences its response to external stress. Here we investigate the effect of uniaxial compression stress on the mechanical stability of MoS_2. We consider separately the zigzag and the arm-chair directions and fixed temperature to 10 K. The outer-row atoms are fixed during the compression steps which are indicated in Fig. 1 by the rectangular areas. The compression rate was taken to be $\mu = 0.5$ m/s (for more details see our previous studies [38,39]) which is small enough to guarantee that the system is in equilibrium during the whole compression process. The critical strain varies with applied compression rate and system size [28]. Recently, Jiang *et al.* studied the buckling of single-layer MoS_2 under uniaxial compression using parametrized Stillinger–Weber potential for MoS_2 [40]. In this section we restrict ourselves to those aspects that were not investigated in Ref. [28].

Figure 4(a) shows the variation of $\langle h^2 \rangle$ with applied uniaxial strain, which was determined by using $\epsilon = \mu t / l$ where t is the time (after starting the compression) and l is the initial length in the direction of the compression. The buckling transition occurs for 0.60% strain, which is about seven times larger than GE (0.09%) when the stress is applied along the zigzag direction and 0.80% which is about five times larger than the one for GE (0.16%) when uniaxial stress is applied along the arm-chair direction. Notice that the buckling transition in MoS_2 is sharper than in GE, which is attributed to the sandwich structure of MoS_2.

The different responses of multilayer MoS_2 on the applied uniaxial stress are displayed in Fig. 4(c). Here, MoS_2 flakes with dimension $l_x \times l_y = 14 \times 14$ nm^2 are considered. It is clear that the single layer becomes buckled at smaller strains as compared with the cases of bi-, tri-, and four-layer MoS_2 for which the buckling transition takes place at 1.5%, 1.8%, and 1.85%, respectively. In particular, tri- and four-layer MoS_2 are close to each other and therefore they approach the limit of bulk MoS_2.

Uniaxial stress simulations can also be used to estimate the Young's modulus. The results for applied stress in the longitudinal (arm-chair direction) and lateral (zigzag direction) directions are shown in Fig. 4(d). The Young's modulus is found by fitting the total energy (per unit area) to the quadratic function

$$E_T = E_0 + \tfrac{1}{2} Y \epsilon^2, \tag{6}$$

where Y is the Young's modulus of the system. Using the aforementioned fitting process, Y is calculated for a flake

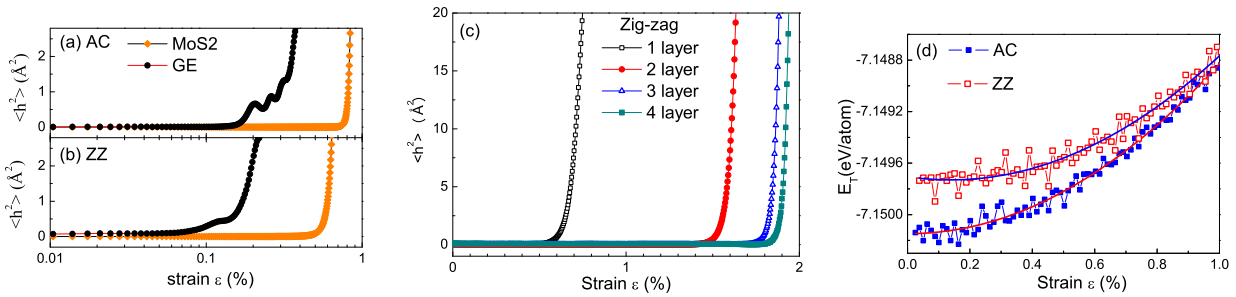

FIG. 4. (Color online) Variation of $\langle h^2 \rangle$ in SL MoS_2 with applied uniaxial stress along (a) arm-chair and (b) zigzag directions. For comparison we show also the corresponding results for graphene. (c) $\langle h^2 \rangle$ of single-, bi-, tri-, and four-layer MoS_2 versus uniaxial strain. (d) Variation of the total energy with uniaxial strain for MoS_2 along arm-chair (blue) and zigzag (red) directions.

with arm-chair and zigzag MoS_2 to be 149 and 148 N/m, respectively, which are values between the recent density functional theory (DFT) result [41,42] of 130 N/m and the experimental value 180 ± 60 N/m [43]. Notice that the Young's modulus of graphene is 340 N/m, which is 2.25 times larger than that of MoS_2.

Notice that, since graphene is a one-atom-thick structure, it is extremely soft in the out-of-plane direction. The latter results in much lower bending modulus than MoS_2 [44]. This is the reason for higher $\langle h^2 \rangle$ in Fig. 2(a) for graphene with respect to MoS_2. However, the in-plane stiffness of graphene because of strong in-plane sp^2 bonds is expected to be much larger than that of MoS_2.

We also studied the effect of vacancies on the buckling transition. Notice that vacancies alter the structure of MoS_2 and change the internal bonds between atoms. This results in a change of the response of the system to any external force simply because the stiffness of the system is reduced even for a few vacancies [45,46]. Recently, Komsa *et al.* [47] studied sulfur vacancies in monolayer MoS_2 under electron irradiation by using high-resolution transmission electron microscopy. These single vacancies are mobile under the electron beam and tend to agglomerate into lines, where the direction of line defects is sensitive to applied uniaxial stress. Figures 5(a) and 5(b) present the vacancy lines perpendicular and parallel to the applied uniaxial stress, respectively. The buckling transition for staggered double-vacancy lines (which are more favorable in experiments) perpendicular and parallel to the applied stress occurs for 0.4% and 0.6% strain (see Fig. 6) where the latter is close to the pristine system.

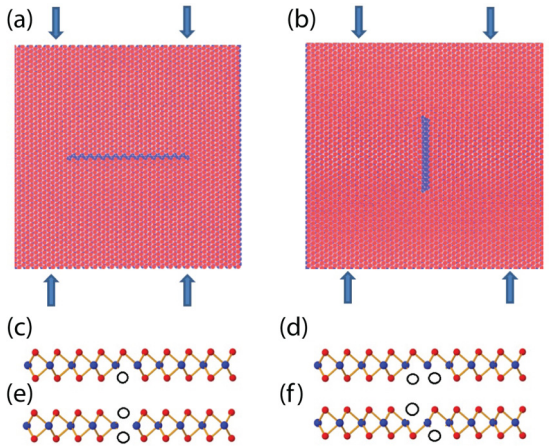

FIG. 5. (Color online) (a) Perpendicular (b) parallel vacancy lines with applied uniaxial stress along zigzag direction. Various models for the (c) single-vacancy line, (d) two neighboring vacancy lines in the same S layer, (e) two vacancy lines coinciding in top and bottom layers, and (f) two vacancies in staggered configuration.

V. MELTING BEHAVIOR

We investigate now the microscopical characteristics of the melting process of single-layer MoS_2. Due to the large simulation time for each temperature we considered here a smaller square-shaped computational unit cell having $N = 7290$ (Mo = 2430 and S = 4860) atoms. The simulations were performed in the NPT ($P = 0$) ensemble with periodic boundary conditions. Temperature was maintained by the Nosé–Hoover thermostat and the MD time step was taken to be 0.1 fs.

We first analyze the case of single-layer MoS_2 and separately keep track of the Mo and S potential-energy contribution. In Figs. 7(a) and 7(b), we show two snapshots of the system before and during melting, respectively. The melting temperature $T_m = 3700$ K is confirmed by the Lindemann parameter γ [Fig. 7(c)] for only the Mo atoms and their nearest neighbors. γ increases linearly as temperature increases and diverges at melting. Figures 8(a) and 8(b) show the variation of the potential energy per atom with time for Mo and S atoms,

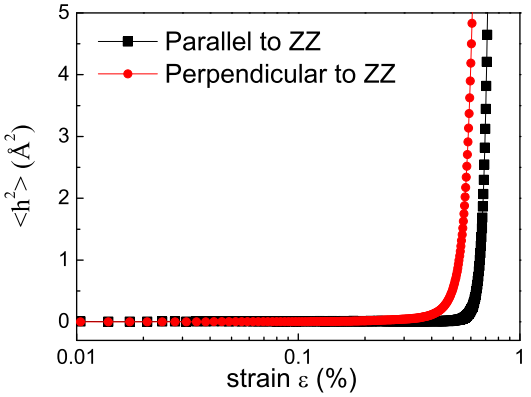

FIG. 6. (Color online) Variation of $\langle h^2 \rangle$ in SL MoS_2 for perpendicular and parallel vacancy lines with applied uniaxial stress along zigzag direction.

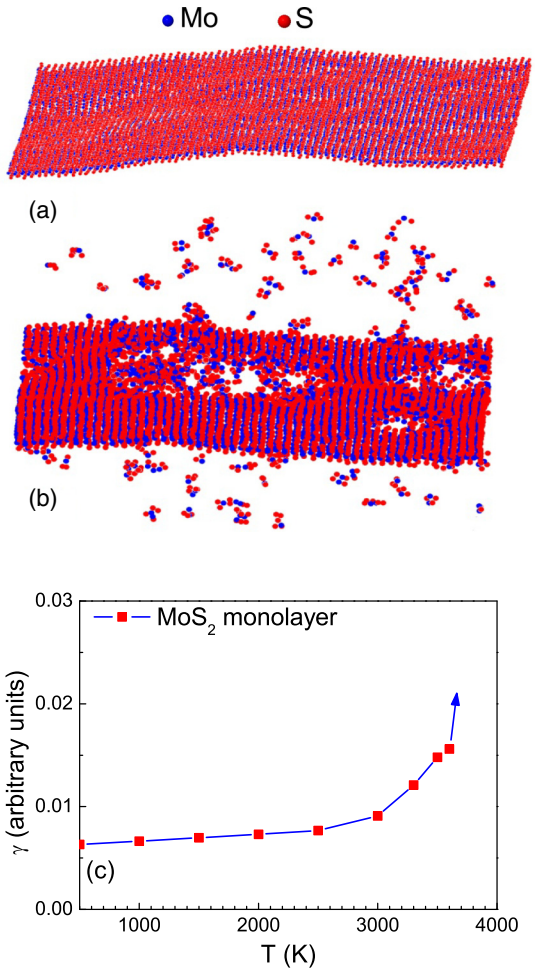

FIG. 7. (Color online) Two snapshots of our MD simulation for the melting of MoS_2 which were taken (a) before melting at 3600 K, and (b) during melting at 3700 K. (c) Modified Lindemann parameter γ versus temperature.

i.e., E_{Mo} and E_{S}, respectively, at 3600 and 3700 K. The sharp increase (decrease) in E_{Mo} (E_{S}) is a signature of melting at $T_m \sim 3700$ K. After melting, the Mo atoms remain bonded to the S atoms and form small molecules which is the reason for the observed increase and decrease of the energy in Figs. 8(a) and 8(b). The larger reduction in E_S indicates that the S atoms prefer to be bonded to the Mo atoms rather than to result in free S atoms.

The radial distribution function (rdf) of Mo-Mo shows that, before melting, there is a sharp peak around 3.2 Å that, after melting, is shifted to the range 2.1–2.5 Å, which is the distance between Mo atoms in small MoS clusters [see Fig. 8(c)]. However, the Mo-S rdf in Fig. 8(d) shows that, after melting, there are only two peaks around 2.2 and 3.2 Å, which are due to the formation of Mo-S and Mo-S_2 clusters, respectively. In contrast to graphene where, after melting, the sample turns into random chains of carbon [48,49], SL MoS_2 transits to a phase consisting of MoS_X clusters. Thus at melting, atoms fluctuate around their equilibrium position, the interatomic Mo-Mo bonds are broken, and Mo becomes free and forms clusters with S atoms.

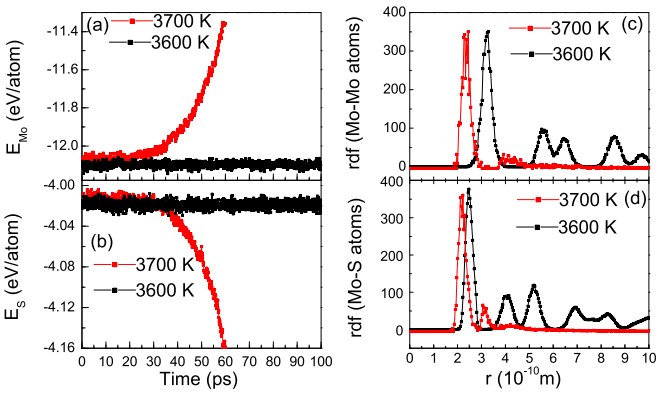

FIG. 8. (Color online) The variation of the potential energy with time of (a) Mo and (b) S atoms before and after melting. In panels (c) and (d) we show the variation of the radial distribution function of Mo-Mo atoms and Mo-S atoms, respectively.

Previously it was found in the presence of helium gas at 1 bar pressure that the melting of bulk MoS_2 occurred around 1853–1895 K depending on the rate of heating [50]. It was found that, at high heating rate, MoS_2 began to decompose into MoS_3 and sulfur gas starting from the solid phase. At lower rates the evaporation losses increased markedly, and MoS_2 was converted into the solid Mo_2S_3 and Mo gas which is a mixture composed of variable amounts of the phases identified chemically and structurally. It was shown that the helium-gas pressure had an influence on the melting temperature. Our results show almost a factor-of-two-higher melting temperature. The reasons for this substantially larger melting temperature may be the presence of helium gas in the experiment, the presence of defects (see Fig. 9), dislocations in the experimental sample, and the weak vdW interaction between layers. Recently, by using high-resolution electron microscopy imaging, the atomic structure and morphology of grain boundaries in MoS_2 have been reported [13]. As we show in Fig. 9, any kind of vacancy in the system reduces the melting temperature. In multilayer MoS_2 the melting starts at the outer layer, also known as "surface melting," while in single layer the melting occurs when the bonds between Mo and S are broken. We also calculated the melting of bilayer

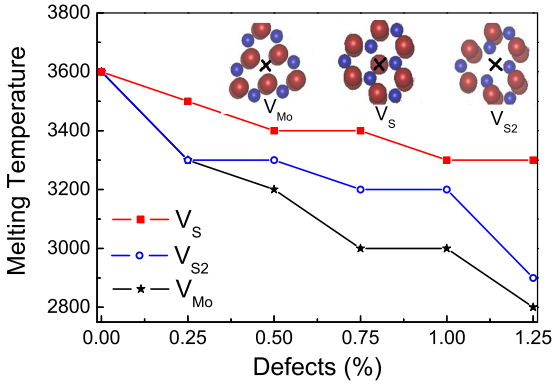

FIG. 9. (Color online) Melting temperature of MoS_2 as function of the percentage of vacancies for different vacancy defects; namely, V_{S2}, V_{MoS3}, and V_{MoS6}. The cross symbols in the insets indicate the missing atom in each structure.

and trilayer MoS_2 and found a similar melting temperature as for single-layer MoS_2. Nevertheless, the melting problem of MoS_2 should be studied systematically by performing tests using different potentials as well as by studying the size effect. We emphasize that, by using any bond-order-type potential, the same order of melting temperature is found which is not expected to be responsible for the factor-of-two difference in melting temperature between bulk MoS_2 and SL MoS_2. It is also important to note that the timescale in our MD simulation is restricted to a maximum of nanoseconds which will lead to an overestimation of the melting temperature, while a real melting phenomena occurs in seconds.

It is worthwhile to study the effect of atomic vacancies in MoS_2 on the melting temperature. We performed several simulations for MoS_2 with different percentages of vacancies (Mo, S, S2) [20] randomly distributed along the sample. The presence of atomic defects in the MoS_2 sheet makes it less stiff and consequently results in a lowering of the melting temperature as can be observed in Fig. 9. It is clear that monosulfur vacancies (V_S), which are usually observed in experiments due to their lower formation energy, has little impact on the melting in comparison to disulfur vacancies (V_{S2}) and V_{Mo}. We can conclude that the presence of V_{Mo}-type defects makes MoS_2 thermally more unstable than the other type of vacancies. Therefor,e missing either Mo or S atoms reduces the melting temperature significantly. This may only indicate that the experimental sample in Ref. [50] is not perfect.

VI. CONCLUSION

Different thermal and mechanical properties of multilayer MoS_2 were investigated by using atomistic simulations. The melting temperature of MoS_2 was found to be very weakly dependent of the number of layers and is lower than the one for graphene. MoS_2 transits quickly to a phase with MoS_X clusters without the appearance of random coils unlike graphene and graphite. The buckling transition in MoS_2 under uniaxial compression is independent of the direction of the applied stress which is also different from graphene. We found that the sandwich structure of MoS_2 makes it a less-stiff material with respect to graphene and it was found to affect different physical properties. MoS_2 is more sensitive to temperature and less energy is needed to excite vibrational modes. The buckling transition is sharper as compared to that of graphene and occurs at substantially larger values of strain. We found that perfect MoS_2 has a higher melting temperature than those systems with defects. The melting temperature of MoS_2 and of MoS_2 with grain boundaries demands more theoretical and experimental studies by using different sizes of computational unit cells and very long MD simulation times, which is beyond the aim of the present study.

ACKNOWLEDGMENTS

This work is supported by the ESF-Eurographene project CONGRAN, the Flemish Science Foundation (FWO-Vl), and the Methusalem Foundation of the Flemish Government. We acknowledge funding from the FWO (Belgium)-MINCyT (Argentina) collaborative research project. We would like to thanks Prof. Douglas E. Spearot [26] for giving us the implemented parameters of Mo-S in LAMMPS.

[1] V. V. Ivanovskaya, A. Zobelli, A. Gloter, N. Brun, V. Serin, and C. Colliex, Phys. Rev. B **78**, 134104 (2008).
[2] S. Lebègue and O. Eriksson, Phys. Rev. B **79**, 115409 (2009).
[3] A. Kuc, N. Zibouche, and T. Heine, Phys. Rev. B **83**, 245213 (2011).
[4] A. Ramasubramaniam, D. Naveh, and E. Towe, Phys. Rev. B **84**, 205325 (2011).
[5] M. Topsakal and S. Ciraci, Phys. Rev. B **85**, 045121 (2012).
[6] Y. D. Ma, Y. Dai, W. Wei, C. W. Niu, L. Yu, and B. B. Huang, J. Phys. Chem. C **115**, 20237 (2011).
[7] R. H. Friend and A. D. Yoffe, Adv. Phys. **36**, 1 (1987).
[8] K. K. Kam and B. A. Parkinson, J. Phys. Chem. **86**, 463 (1982).
[9] K. F. Mak, C. Lee, J. Hone, J. Shan, and T. F. Heinz, Phys. Rev. Lett. **105**, 136805 (2010).
[10] A. Splendiani, L. Sun, Y. Zhang, T. Li, J. Kim, C.-Y. Chim, G. Galli, and F. Wang, Nano Lett. **10**, 1271 (2010).
[11] A. Castellanos-Gomez, R. Roldan, E. Cappelluti, M. Bucema, F. Guinea, H. S. J. van der Zant, and G. A. Steele, Nano Lett. **13**, 5361 (2013).
[12] Y. Cai, J. Lan, G. Zhang, and Y-W. Zhang, Phys. Rev. B **89**, 035438 (2014).
[13] S. Najmaei, Z. Liu, W. Zhou, X. Zou, G. Shi, S. Lei, B. I. Yakobson, J.-C. Idrobo, P. M. Ajayan, and J. Lou, Nat. Mater. **12**, 754 (2013).
[14] A. M. van der Zande, P. Y. Huang, D. A. Chenet, T. C. Berkelbach, Y. You, G.-H. Lee, T. F. Heinz, D. R. Reichman, D. A. Muller, and J. C. Hone, Nat. Mater. **12**, 554 (2013).
[15] J. C. Meyer, A. Chuvilin, G. Algara-Siller, J. Biskupek, and U. Kaiser, Nano Lett. **9**, 2683 (2009).
[16] C. Jin, F. Lin, K. Suenaga, and S. Iijima, Phys. Rev. Lett. **102**, 195505 (2009).
[17] H.-P. Komsa, J. Kotakoski, S. Kurasch, O. Lehtinen, U. Kaiser, and A. V. Krasheninnikov, Phys. Rev. Lett. **109**, 035503 (2012).
[18] G. Algara-Siller, S. Kurasch, M. Sedighi, O. Lehtinen, and Ute Kaiser, Appl. Phys. Lett. **103**, 203107 (2013).
[19] R. Zan, Q. M. Ramasse, R. Jalil, T. Georgiou, U. Bangert, and K. S. Novoselov, ACS Nano **7**, 10167 (2013).
[20] W. Zhou, X. Zou, S. Najmaei, Z. Liu, Y. Shi, J. Kong, J. Lou, P. M. Ajayan, B. I. Yakobson, and J. C. Idrobo, Nano Lett. **13**, 2615-2622 (2013).
[21] S. Costamagna, M. Neek-Amal, J. H. Los, and F. M. Peeters, Phys. Rev. B **86**, 041408(R) (2012).
[22] S. K. Singh, M. Neek-Amal, S. Costamagna, and F. M. Peeters, Phys. Rev. B **87**, 184106 (2013).
[23] S. K. Singh, S. G. Srinivasan, M. Neek-Amal, S. Costamagna, A. C. T. van Duin, and F. M. Peeters, Phys. Rev. B **87**, 104114 (2013).

[24] T. Liang, S. R. Phillpot, and S. B. Sinnott, Phys. Rev. B **79**, 245110 (2009).
[25] T. Liang, S. R. Phillpot, and S. B. Sinnott, Phys. Rev. B **85**, 199903(E) (2012).
[26] J. A. Stewart and D. E. Spearot, Modell. Simul. Mater. Sci. Eng. **21**, 045003 (2013).
[27] D. W. Brenner, O. A. Shenderova, J. A. Harrison, S. J. Stuart, B. Ni, and S. B. Sinnott, J. Phys.: Condens. Matter **14**, 783 (2002).
[28] J. W. Jiang, Nanotechnology **25**, 355402 (2014).
[29] http://lammps.sandia.gov
[30] S. Plimpton, J. Comput. Phys. **117**, 1 (1995).
[31] F. A. Lindemann, Phys. Z. **11**, 609 (1910).
[32] V. M. Bedanov, G. V. Gadiyak, and Yu. E. Lozovik, Phys. Lett. A **109**, 289 (1985).
[33] V. M. Bedanov and F. M. Peeters, Phys. Rev. B **49**, 2667 (1994).
[34] X. H. Zheng and J. C. Earnshaw, Europhys. Lett. **41**, 635 (1998).
[35] D. Nelson, T. Piran, and S. Weinberg, *Statistical Mechanics of Membrane and Surface* (Word Scientific, Singapore, 2004).
[36] A. Fasolino, J. H. Los, and M. I. Katsnelson, Nat. Mater. **6**, 858 (2007).
[37] S. Costamagna and A. Dobry, Phys. Rev. B **83**, 233401 (2011).
[38] M. Neek-Amal and F. M. Peeters, Phys. Rev. B **82**, 085432 (2010).
[39] M. Neek-Amal and F. M. Peeters, J. Phys.: Condens. Matter **23**, 045002 (2011).
[40] J. W. Jiang, H. S. Park, and T. Rabczuk, J. Appl. Phys. **114**, 064307 (2013).
[41] R. C. Cooper, C. Lee, C. A. Marianetti, X. Wei, J. Hone, and J. W. Kysar, Phys. Rev. B **87**, 035423 (2013).
[42] R. C. Cooper, C. Lee, C. A. Marianetti, X. Wei, J. Hone, and J. W. Kysar, Phys. Rev. B **87**, 079901(E) (2013).
[43] S. Bertolazzi, J. Brivio, and A. Kis, ACS Nano **5**, 9703 (2011).
[44] J. W. Jiang, arXiv:1408.0437.
[45] M. Neek-Amal and F. M. Peeters, Phys. Rev. B **81**, 235437 (2010).
[46] M. Neek-Amal and F. M. Peeters, Appl. Phys. Lett. **97**, 153118 (2010).
[47] H. P. Komsa, S. Kurasch, O. Lehtinen, U. Kaiser, and A. V. Krasheninnikov, Phys. Rev. B **88**, 035301 (2013).
[48] K. V. Zakharchenko, A. Fasolino, J. H. Los, and M. I. Katsnelson, J. Phys.: Condens. Matter **23**, 202202 (2011).
[49] S. K. Singh, S. Costamagna, M. Neek-Amal, and F. M. Peeters, J. Phys. Chem. C **118**, 4460 (2014).
[50] I. G. Vasilyeva and R. E. Nikolaev, J. Alloys Compd. **452**, 89 (2008).